Redox properties and catalytic behavior of praseodymium-modified $(Ce–Zr)O_2$ solid solutions in three-way catalysts

Wendong Wang, Peiyan Lin *, Yilu Fu, and Gengyu Cao

Department of Chemical Physics, University of Science and Technology of China, Hefei 230026, PR China

Received 8 January 2002; accepted 28 March 2002

The three-way catalyst promoters $(Ce–Zr)O_2$, $(Pr–Ce–Zr)O_2$ and $(Pr–Zr)O_2$ were prepared by the sol-gel method. The reduction/oxidation behavior of these mixed oxides was compared. It is shown that the formation of $(Pr–Zr)O_2$ cubic solid solution at high temperature up to 800 °C makes it more reducible, and that the ternary solid solution that formed in $(Pr–Ce–Zr)O_2$ mixed oxides plays an important role in the reduction process. The catalytic performance tests reveal that the introduction of a small amount of praseodymium into $(Ce–Zr)O_2$ favors the light-off temperature of C_3H_6 and NO and the effectiveness for NO conversion at the lean region.

KEY WORDS: three-way catalyst; praseodymium; $(Ce–Zr)O_2$ solid solution; redox properties; sol-gel method.

1. Introduction

CeO_2 is present in the majority of formulations of three-way catalysts (TWCs) due to its well-known multiple effects on the catalyst state and performance, such as: (i) stabilization of the precious metals dispersion and the alumina support [1]; (ii) promotion of the water–gas shift reaction and the steam-reforming reaction [2]; (iii) suppression of the strong rhodium–alumina interaction [3]. The primary function of CeO_2 in the TWCs is to provide oxygen-storage capacity (OSC), acting as an efficient "oxygen buffer" to undergo effective reduction/oxidation cycles by shifting between CeO_2 under oxidizing conditions (oxygen storage) and Ce_2O_3 under reducing conditions (oxygen release), respectively. Thus, the TWCs' highest conversions of the carbon monoxide (CO), hydrocarbons (HCs) and nitrogen oxides (NO_x) are attained around the stoichiometric air/fuel value [4].

However, a major shortcoming of CeO_2 is that significant deactivation of the redox couple occurs due to the sintering of CeO_2 particles and the reactions between CeO_2 and γ-alumina support or active precious metals when it is performed at high temperature in the driving conditions [5,6]. Then the OSC decreases and the activity of the catalyst declines.

An approach of incorporating lower valent ions such as the rare earths (La, Y, etc.) [7,8] into the CeO_2 lattice has been suggested to enhance the resistance to sintering and to increase the OSC, due to the creation of a corresponding number of anion vacancies. More recently, it has been reported that doping Zr^{4+} into the CeO_2 cubic lattice leads to improvements in the activities and thermal stability of the catalysts [9–11]. Various synthetic routes of $(Ce–Zr)O_2$ were reported such as high-energy vibratory ball at room temperature [12]; the scay-ICP technique resulting in high dispersion between ultrafine CeO_2 and ZrO_2 particles [13]; sol-gel techniques (organic or inorganic sol precursors) and supercritical drying to give nanosized $(Ce–Zr)O_2$ [14–16].

There are some other reducible oxides that have not been experimented within detail as an oxygen-storage promoter or as the third ions doping into the $(Ce–Zr)O_2$. These kinds of oxide possess some similar properties to that of cerium. For example, praseodymium is next to cerium in the Periodic Table and also possesses stable multiple oxidation states; yet praseodymium does not appear to be an effective replacement for cerium as an oxygen-storage component. One major reason for this is related to the great difference in the reactivities of cerium and praseodymium with alumina. Praseodymium, due to its relatively low stability, reacts with alumina at temperature above 600 °C in air and forms inert aluminates, whereas cerium remains stable up to at least 1100 °C. Mixed-valence rare earth oxides (Pr_6O_{11} and Tb_4O_7) are oxides in which +3 and +4 cations coexist at equilibrium under ambient conditions. The formula of the stable praseodymium oxide is Pr_6O_{11} ($Pr_2O_3{\cdot}4PrO_2$) where 1/3 of the cations are already in the trivalent state. In the cerium–praseodymium mixed oxides, the defects are induced by incorporation of foreign cations (Pr^{3+}) that have a lower valence than those of the Ce^{4+} that they replace. Mixed Pr–Ce oxides have been examined to determine the overall amount of removable oxygen under conditions of desorption, reduction, and oxidation [17]. Narula *et al.* [18] synthesized high-surface-area $Pr_y–ZrO_2$ mixed oxides, crystallized in the cubic fluorite structure, over a wide range composition by sol-gel processing. Although praseodymium (or stabilized praseodymium-based mixed

* To whom correspondence should be addressed.
E-mail: fulin@ustc.edu.cn

1011-372X/02/0900-0019

oxides) may be proved unsuitable as a direct replacement for cerium-based oxygen-storage components, its ability to release a large amount of O_2 at relatively low temperature may be useful in formulating rapid light-off catalysts for lowering cold-start emissions [19].

The advent of zirconia stabilization, however, raises the possibility that the thermal instability for praseodymium may be avoided. The characterizations and the reduction/oxidation properties of the praseodymium–zirconia and cerium–praseodymium–zirconia materials have not been previously reported in detail. In the present work, the TWC promoters $(Ce–Zr)O_2$, $(Pr–Ce–Zr)O_2$ and $(Pr–Zr)O_2$ were prepared by the sol-gel route with some special procedures. These mixed oxides were characterized by XRD, EXAFS, H_2–TPR and OSC measurement in detail. The catalytic performance was also measured for the fully formulated Pt, Pd and Rh three-way catalysts containing these kinds of promoters.

2. Experimental

2.1. Sample preparation

The $(Ce–Zr)O_2$ and $(Pr–Zr)O_2$ mixed oxides were synthesized from mixed aqueous solutions of $Ce(NO_3)_3{\cdot}6H_2O$ (or $Pr(NO_3)_3$) and $ZrO(NO_3)_2{\cdot}2H_2O$ with a Ce/Zr (or Pr/Zr) atomic ratio of 1.94. The solutions were mixed with the equivalent of citric acid. The mixed solution was stirred and evaporated until it became a transparent viscous sol. The sol was dried at 120 °C in an oven overnight and then calcined at 500 °C for 4 h to obtain the mixed oxide.

The $(Pr–Ce–Zr)O_2$ mixed oxides were prepared in two steps. At first, the Pr^{3+} and Zr^{4+} cations in the aqueous solution were mixed with the equivalent of citric acid and a transparent solution formed as mentioned above; then the $(Ce–Zr)O_2$ solid-solution powder was mixed with the fluid sol. The mixture was stirred and evaporated, and then dried and calcined at 500 °C for 4 h to obtain a series of $(Pr–Ce–Zr)O_2$ mixed oxides. The doping compositions, denotations and surface areas of the mixed oxides are shown in table 1. The doping compositions were calculated by assuming that all the Pr^{n+} were +4 valence in the mixed oxides.

The low precious metal (denoted as PMs in this article) loading catalysts were prepared by wet impregnation of support γ-alumina-containing promoters of La_2O_3 and $(Pr–Ce–Zr)O_2$ (or $(Ce–Zr)O_2$) in pellets of 40–60 mesh. Both the 30 wt% of La_2O_3 and 30 wt% of $(Pr–Ce–Zr)O_2$ (or $(Ce–Zr)O_2$) were mixed with γ-alumina prior to the impregnation of PMs. Co-impregnation of the precious metal salts $H_2PtCl_6{\cdot}6H_2O$, $PdCl_2$ and $RhCl_3{\cdot}3H_2O$ aqueous solution was adopted for all the catalysts. The total PM loading is 0.40 wt% on γ-Al_2O_3, including Pt 0.15 wt%, Pd 0.20 wt% and Rh 0.05 wt%. After co-impregnation, the catalysts were dried and then calcined in air at 500 °C for 2 h. Fresh catalysts were reduced under hydrogen at 450 °C for 1 h. The aged condition is calcination at 850 °C for 2 h in atmosphere. The detailed pretreatment condition was in a previous publication [20].

Table 1
Doping composition and BET surface area of the samples

Denotation	Doping composition	Surface area (m^2/g)	
		500 °C, 2 h	850 °C, 2 h
CZ	$Ce_{0.6}Zr_{0.34}O_2$	67.1	37.5
PCZ(1/21)	$Pr_{0.03}Ce_{0.63}Zr_{0.34}O_2$	72.5	42.8
PCZ(1/10)	$Pr_{0.06}Ce_{0.60}Zr_{0.34}O_2$	76.6	40.3
PCZ(1/5)	$Pr_{0.11}Ce_{0.55}Zr_{0.34}O_2$	90.9	37.2
PZ	$Pr_{0.66}Zr_{0.34}O_2$	6.5	3.7

For comparison purposes, three different procedures were used to prepare the catalysts containing $(Pr–Zr)O_2$: (a) PM–PZ(a) was prepared as mentioned above; (b) for PM–PZ(b), the mixture of $(Pr–Zr)O_2$, La_2O_3 and γ-alumina was calcined at 850 °C prior to the impregnation of PMs; (c) for PM–PZ(c), the $(Pr–Zr)O_2$ was calcined at 850 °C and then mixed with La_2O_3 and γ-alumina prior to the impregnation of PMs.

2.2. Determination of characteristics

X-ray diffraction (XRD) patterns were recorded on a D/MAX-γA rotatory target diffractometer, using Cu K_α radiation ($\lambda = 0.15418$ nm) as X-ray source, operated at 40 kV and 100 mA. The crystalline phases were identified by comparison with the reference data from the International Center for Diffraction Data (ICDD).

Surface-area measurements were determined on a Sibata system using the BET equation.

The spectra of extended X-ray absorption fine structure (EXAFS) were measured at the beamline of 4WIB of the Beijing Synchrotron Radiation Facility (BSFR). The storage ring was operated at 2.2 GeV with a typical current of 50 mA. Fixed-exit Si(111) flat double crystals were used as the monochromator. The spectra were recorded in transmission mode with ionization chambers filled with argon. All the samples were measured at the Zr-K edge. Spectra of m-ZrO_2 and $BaZrO_3$ were collected as reference compounds. Data analysis was performed following a standard procedure [21].

The EXAFS signals multiplied by k^3 were Fourier transformed in the limits 3.00–12.70 $Å^{-1}$ for Zr, and then the peaks present in R space were obtained.

Temperature-programmed reduction (TPR) experiments were carried out in a conventional system equipped with a thermal conductivity detector. The weight of the sample was 200 mg. After pretreatment in a flow of pure Ar at 500 °C, the reduction was carried out in a flow of H_2 (5%) in Ar (30 ml min^{-1}) from 120 to 800 °C with a linear heating rate of 10 °C min^{-1}. The

amount of H_2 uptake in the TPR was estimated from integrated peak areas by comparison with those obtained by using CuO as a standard.

Oxygen-storage capacity was measured by the pulse technique in the same equipment as used for the TPR experiment. After the TPR, the sample was outgassed under an Ar flow at 800 °C for 1 h and cooled down to 400 °C. The oxygen uptake was measured at 400 °C by injecting pulses of O_2 (0.13 ml) into the flow of Ar (20 ml min^{-1}) passing over the sample until no oxygen consumption could be detected.

A quadrupole mass spectrometer (Balzers OmniStar GSD 300 O2) was used for NO temperature-programmed desorption (TPD). The catalyst (200 mg) was pretreated in Ar flow at 500 °C for 1 h and then cooled down to 200 °C, where the adsorption was carried out in a flow of NO (1%) and O_2 (5%) in Ar for 1 h. The catalyst was outgassed under Ar flow at this temperature for 2 h and then cooled down to room temperature. TPD measurements were carried out from room temperature to 600 °C with a linear heating rate of 10 °C min^{-1}.

2.3. Catalytic performance test procedure

2.3.1. Light-off temperature

Reaction was carried out in a conventional flow-bed reactor and 600 mg of the catalyst was used. A complete gas mixture (e.g. CO 1.50 vol%, NO 1000 ppm, C_3H_6 1500 ppm and O_2 1.38 vol% with N_2 balanced) was passed over the catalyst at a space velocity of 30 000 h^{-1}. The composition of the reactant mixture was maintained constant throughout the catalytic test at $S = 1.00$, where the stoichiometric number S is defined as

$$S = \frac{2[O_2] + [NO]}{[CO] + 9[C_3H_6]}.$$

The results of this test are given in terms of light-off temperature, at which 50% of the reactants have been converted.

2.3.2. Conversions with various S values at constant temperature

During this test, the content of oxygen in the reactant mixture altered, so that the S values changed from 0.96 to 1.07, while the reaction temperature remained constant at 400 °C. When the S value was lower or greater than unity ($S = 1.00$), the reaction was carried out under reducing or oxidizing conditions, respectively.

3. Results and discussion

3.1. Characterization of the mixed oxides

The doping composition and the BET surface area of the mixed oxides are listed in table 1. The CZ sample shows a much higher surface area than that of the PZ sample. In spite of the low surface area of the PZ sample, the addition of praseodymium in the scale of this work does not reduce the CZ sample's surface area. The PCZ samples exhibit higher surface area than that of the CZ sample. An increase of the dopant praseodymium content from 3 mol% to 11 mol% favors an increase of surface area from 72.5 m^2/g to 90.9 m^2/g compared with the undoped CZ sample's 67.1 m^2/g. It seems that the introduction of praseodymium to the CZ sample can not only lead to a high dispersion of praseodymium itself on the CZ surface, but can also stabilize the CZ surface area to some extent after the calcination at 500 °C. After the calcination at the higher temperature of 850 °C, the surface area decreases for all the samples.

In the case of the binary system ($Ce_xZr_{1-x}O_2$), there are three possible structures: monoclinic, tetragonal and cubic [10,14,23]. Vidmar *et al.* [14] have also mentioned that there are three different tetragonal phases (t, t' and t'') for the binary system. The t form is a stable one formed through a diffusional phase decomposition, the t' form is a metastable phase obtained through a diffusionless phase transition, while the t'' form is intermediate between the t'-form and the cubic phase. The t'' phase shows no tetragonality, and it exhibits an oxygen displacement from ideal fluorite sites. The t''-phase is generally referred to as cubic phase.

Figure 1 shows the XRD patterns of the CZ, PCZ(1/5) and PZ samples, and those of CeO_2 and Pr_6O_{11} as the references. Both CeO_2 and Pr_6O_{11} exhibit cubic phase with different lattice parameters (table 2). For the CZ sample, only the cubic phase can be observed. It features broad symmetric peaks attributed to the presence of

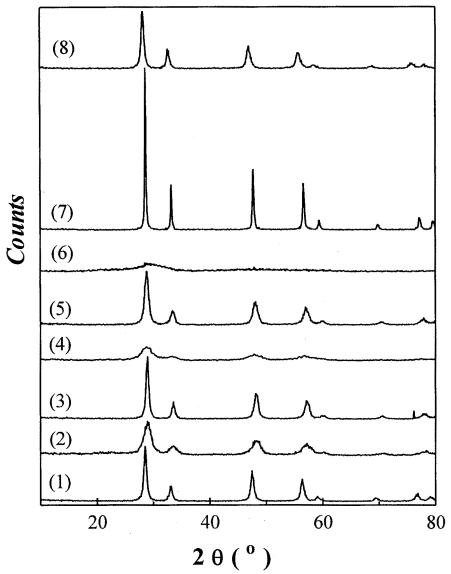

Figure 1. XRD patterns of: (1) CeO_2 (purity of 99.9%); (2) CZ calcined at 500 °C; (3) CZ calcined at 850 °C; (4) PCZ calcined at 500 °C; (5) PCZ calcined at 850 °C; (6) PZ calcined at 500 °C; (7) PZ calcined at 850 °C; (8) Pr_6O_{11} (purity of 99.9%).

Table 2
The lattice parameters of some samples calcined at different temperature

Sample	Lattice parameter (nm)		
	500°C	850°C	Calculated value [a]
CeO_2	0.5418	0.5418	–
Pr_6O_{11}	0.5485	0.5485	–
CZ	0.5404	0.5341	0.5320
PZ	nc	0.5399	0.5387
PCZ(1/5)	0.5371	0.5384	–

nc: noncrystalline.
[a] The lattice parameters were estimated from the linear relation $d_{Ce–Zr}$ [22] = (0.5418 − 0.0002884 × mol% Zr) nm, the mol% Zr = 34 and $d_{Pr–Zr}$ = (0.5485 − 0.0002884 × mol% Zr) nm, the mol% Zr = 34.

small crystallites which are formed after the calcination at 500 °C. With an increase in the calcination temperature to 850 °C, it can be seen that the intensity of the peaks increases and the width of the peaks decreases, which may be due to the sample sintering. Similar patterns are also obtained for the PCZ(1/5) sample. As for the PZ sample, it appears a quite different situation, which features a noncrystalline phase with only one much weaker and broader peak around 28° (2θ) after calcination at 500 °C. With an increase in the calcination temperature, the PZ sample shows the most intense and narrow peaks among all the samples, which implies that the PZ sample experiences a more drastic phase transformation and sintering than the other samples during calcination at 850 °C.

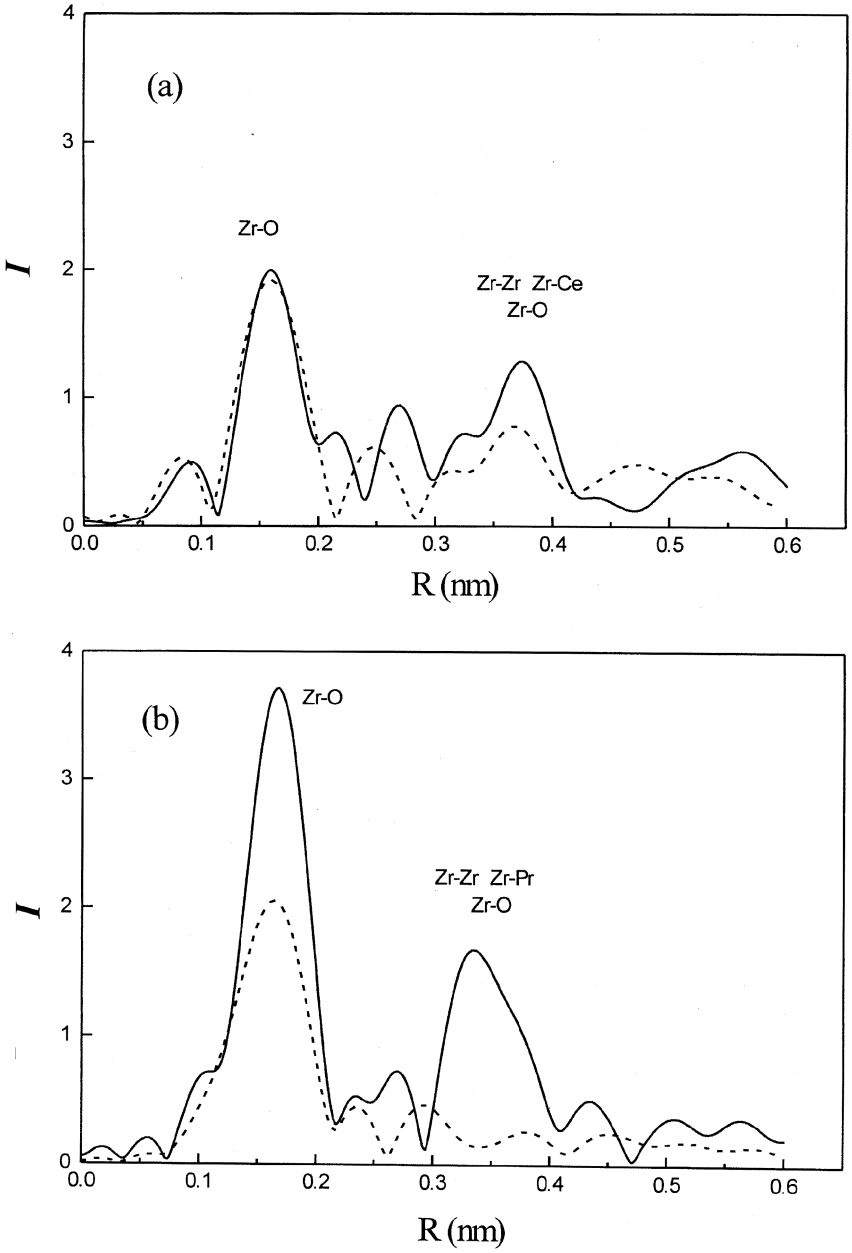

Figure 2. Modulus of the Fourier transform (FT) of the experimental data of (a) CZ; (b) PZ. (····) calcination at 500 °C, (——) calcination at 850 °C.

Compared with CeO_2, shifts of the peak's position were also observed, which represents different lattice parameters of the cubic phase for the samples. The lattice parameters of the samples, estimated from the diffraction peak around 28° (2θ) assigned to the cubic phase (111), are shown in table 2. The CZ sample calcined at 500 °C exhibits a smaller lattice parameter (0.5404 nm) than that of CeO_2 (0.5418 nm), and a much smaller one (0.5341 nm) after calcination at 850 °C. This means the dissolution of Zr^{4+} ions into the CeO_2 lattice and the formation of solid solution, since the radius of Zr^{4+} ion (0.079 nm) is smaller than that of Ce^{4+} ion (0.094 nm). The calculated lattice parameter of the $Ce_{0.66}Zr_{0.34}O_2$ solid solution is 0.5320 nm according to the doping composition [22]. This shows that a more complete formation of solid solution is achieved after calcination at 850 °C than at 500 °C. A similar conclusion can be made for the PZ sample by comparison with Pr_6O_{11}. The PCZ(1/5) sample may reveal a more complex composition. Its lattice parameter (0.5384 nm) is reasonably between those of solid solution CZ and PZ after calcination at 850 °C.

Figure 2(a) reports the modulus of the Fourier transforms of the EXAFS signals for the CZ samples measured at the Zr-*K* edge. The region 1.1–2.4 Å is associated with the Zr–O banding while the region 2.4–4.2 Å is mainly associated with the Zr–M (M = Zr, Ce) interactions. A similar assignment can be made for the PZ samples in figure 2(b). For the two CZ samples calcined at 500 and 850 °C respectively, there is almost no difference at the first shell Zr–O and only a slight change at the second shell Zr–M due to its relatively high thermal stability. However, the PZ sample calcined at 850 °C boosts highly at the first shell Zr–O and there appear Zr–M (M = Zr, Pr) interactions apparently. This indicates that the local structure of the PZ sample undergoes an ordering process during the calcination, which is consistent with the result of XRD patterns of PZ.

3.2. Reduction behavior and oxygen uptake

The H_2–TPR profiles of the samples calcined at 500 °C are plotted in figure 3. The CZ sample features a nonsymmetrical peak at about 572 °C, which is attributed to the reduction of the Ce^{4+} for the $(Ce–Zr)O_2$ solid solution [14]. Doping with praseodymium of 3, 6 and 11 mol% does not change the shape of the main peak significantly. However, by increasing the praseodymium content, the peak shifts upward from 572 to 584 °C, then to 601 °C successively. It seems that doping with praseodymium slightly retards the reduction of the Ce^{4+} for the $(Ce–Zr)O_2$ solid solution. Meanwhile, the increase of the dopant praseodymium content leads to a more apparent reduction peak at 394 °C, which may be attributed to the reduction of the Pr^{4+} for the PCZ samples. The PZ sample does not show an apparent reduction peak until the temperature reaches 600 °C.

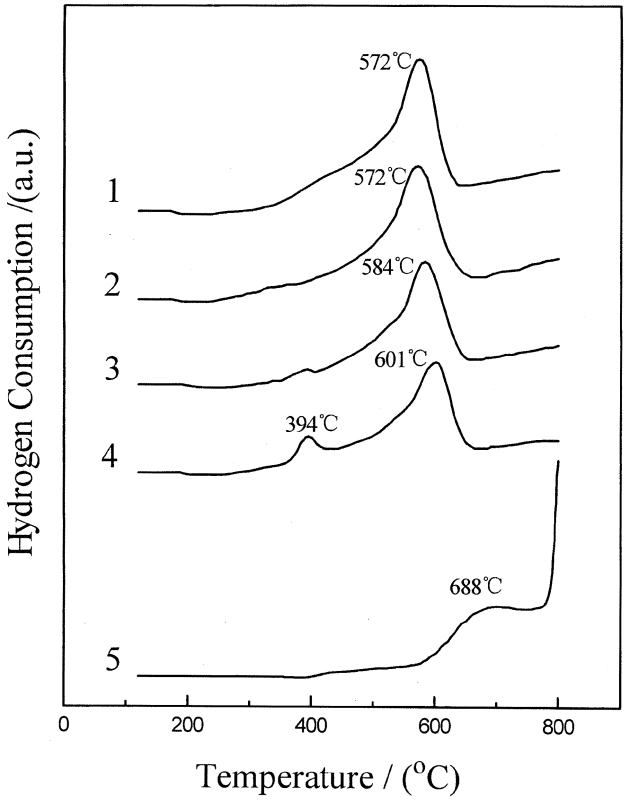

Figure 3. H_2–TPR profiles of a series of $(Ce–Pr–Zr)O_2$ samples calcined at 500 °C: (1) CZ; (2) PCZ(1/21); (3) PCZ(1/10); (4) PCZ(1/5); (5) PZ.

In figure 4, the TPR profiles of the samples calcined at 850 °C are plotted. It shows that the shape of the reduction peak for the CZ sample does not change in comparison with that of the sample calcined at 500 °C, which implies that the $(Ce–Zr)O_2$ solid solution has already formed after calcination at 500 °C. However, two apparent reduction peaks appear for the samples of PCZ. The shape of the peak varies by doping with praseodymium from 3 to 11 mol%. The increase of the dopant praseodymium amount lowers the peak area of the second peak around 560 °C, which is associated with the reduction of the $(Ce–Zr)O_2$ solid solution. On the other hand, the main peaks of the doped samples shift from 516 to 475 °C, then to 453 °C by increasing the praseodymium content. The PZ sample features a broad reduction peak from 300 to 600 °C, and a shoulder at about 635 °C.

Oxygen uptakes at 400 °C measured after reduction are reported in table 3. For comparison, the amount of H_2 consumption in the reduction before the oxygen uptake measurements is included. The values correspond to the oxygen uptake. As pointed out by Cho [24], in the OSC measurement by the pulse method, the oxygen uptake is controlled by the mobility of oxygen at a given temperature rather than by the ultimate oxygen-storage capacity of the support, which is in fact independent of the temperature. For the CZ and three PCZ samples, it can be seen that the H_2 consumption and

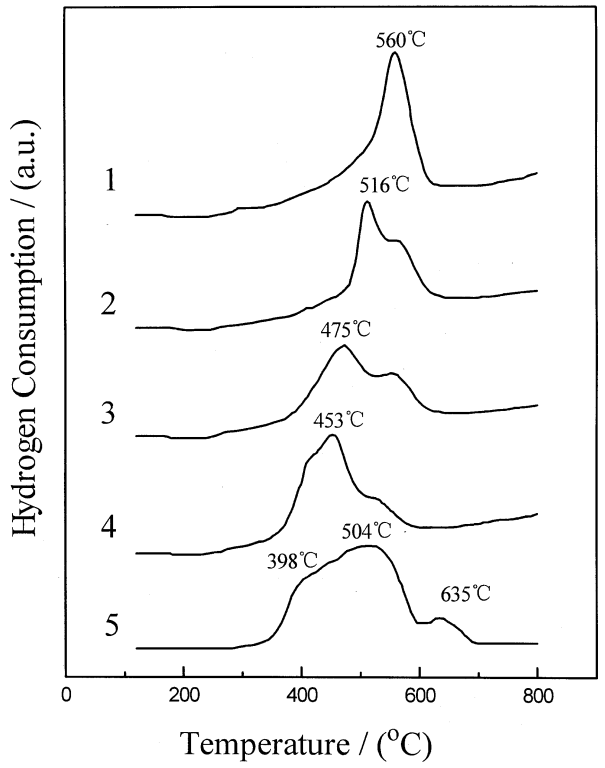

Figure 4. H_2–TPR profiles of a series of $(Ce–Pr–Zr)O_2$ samples calcined at 850 °C: (1) CZ; (2) PCZ(1/21); (3) PCZ(1/10); (4) PCZ(1/5); (5) PZ.

oxygen uptake are almost the same as the calcination temperature increases, while the surface area of the sample greatly decreases (table 1). This indicates that the high values of OSC are independent of the surface area of the samples and must be associated with a bulk redox process. However, H_2 consumption of the PZ sample calcined at 500 and 850 °C is 1.02 and 1.55 mmol g^{-1}, respectively. The latter is about 50% higher than the former.

3.3. *Effects of Pr on the mixed oxides*

The characterization and redox properties reveal that the PZ sample undergoes a more drastic phase transformation than the CZ sample. XRD detects a noncrystalline phase for PZ calcined at 500 °C (figure 1, trace 6) and a cubic phase at 850 °C (figure 1, trace 7). The ordering process is also confirmed by the EXAFS results (figure 2(b)). The TPR profile indicates that the transformation starts at about 600 °C and the $(Pr–Zr)O_2$ cubic solid solution forms at about 800 °C (figure 3, trace 5). After the calcination at 850 °C, the formation of the solid solution makes the PZ sample more reducible and increases oxygen-storage capacity. It features a broad reduction peak from about 300 to 600 °C with larger H_2 consumption (figure 4, trace 5), which may be attributed to a multi-stage reduction due to various x of the PrO_x, where x varies from 2 to 1.5.

Table 3
Hydrogen consumption and oxygen uptake over the samples calcined at different temperature

Sample	H_2 consumption [a] (mmol g^{-1})		O_2 uptake [b] (mmol g^{-1})	
	500 °C	850 °C	500 °C	850 °C
CZ	1.50	1.51	0.74	0.75
PCZ(1/21)	1.47	1.51	0.74	0.76
PCZ(1/10)	1.46	1.50	0.73	0.75
PCZ(1/5)	1.43	1.52	0.72	0.75
PZ	1.02	1.55	0.48	0.78

[a] Standard deviation: ±0.05 m mol H_2 g^{-1}.
[b] Standard deviation: ±0.01 m mol O_2 g^{-1}.

The characterization mentioned above indicates a significant modification of the present solid solutions introduced by Pr. One can be sure that the main phase for the PCZ samples calcined at 500 °C is the phase of $(Ce–Zr)O_2$ solid solution, and some PrO_x and ZrO_2 also exist. No $(Pr–Ce–Zr)O_2$ or $(Pr–Zr)O_2$ solid solution forms at 500 °C. In the TPR profiles, the total H_2 consumption slightly decreases as the praseodymium content increases, which is mainly due to the decrease of Ce^{4+} relative content in the PCZ samples. Besides, the highly dispersed PrO_x and ZrO_2, which were prepared by the sol-gel method, also inhibit the reduction of Ce^{4+} in the $(Ce–Zr)O_2$ and make its reduction peak shift up (figure 3, traces 2, 3 and 4).

After calcination at 850 °C, there is a great change in the phase composition for the PCZ samples. The main reduction peaks of the PCZ samples shift down and the peak attributed to the $(Ce–Zr)O_2$ becomes smaller and smaller by increasing the praseodymium content. Especially for the PCZ(1/5) sample, almost no reduction peak associated with $(Ce–Zr)O_2$ can be identified, while the total H_2 consumption of the three PCZ samples and the CZ sample is at the same level. It is considered that part of the Pr^{4+} may dissolve into the $(Ce–Zr)O_2$ solid solution and a ternary $(Pr–Ce–Zr)O_2$ solid solution forms. Meanwhile, the phases of highly dispersed $(Pr–Zr)O_2$ solid solution formed at 600–800 °C and a small amount of $(Ce–Zr)O_2$ solid solution also exist. Since the oxidized Pr^{4+} ions in the $(Pr–Zr)O_2$ solid solution are more reducible than the Ce^{4+} in $(Ce–Zr)O_2$ solid solution, it is suggested that in the PCZ samples the Ce^{4+} ions may be reduced through the migration of associated oxygen to the Pr^{4+} ions, which makes Ce^{4+} easier to reduce. Therefore, the ternary $(Pr–Ce–Zr)O_2$ solid solution plays an important role in the reduction process. The overall redox cycle efficiency between Ce^{4+} and Ce^{3+} becomes much higher during doping of a small amount of praseodymium into the $(Ce–Zr)O_2$ solid solution.

3.4. *Evaluation of catalytic activities*

The conversions of CO, C_3H_6 and NO dependence on temperature were measured under stoichiometric

Table 4
Catalytic performance for the three-way catalysts

Catalyst	Light-off temperature (°C)						W [a]
	Fresh sample			Aged sample			
	CO	C_3H_6	NO	CO	C_3H_6	NO	
PM–CZ	283.8	286.0	286.4	275.5	303.3	322.6	1.026
PM–PCZ(1/21)	274.6	276.8	276.8	282.1	300.7	315.6	1.027
PM–PCZ(1/10)	274.2	277.1	277.1	311.0	318.8	327.0	1.031
PM–PCZ(1/5)	274.6	277.1	276.5	315.2	331.7	354.5	1.032
PM–PZ(a)	261.4	264.3	265.9	355.6	355.6	360.7	1.031
PM–PZ(b)	278.6	284.1	284.4	315.3	317.3	320.9	1.033
PM–PZ(c)	274.7	277.1	277.4	331.0	333.4	339.0	1.031

[a] The width of the S value at NO conversion(%) $\geq$ 80% under oxidizing conditions ($S \geq 1.00$).

number $S = 1.00$ for all the fresh and aged catalysts, from which the light-off temperatures of CO, C_3H_6 and NO are obtained and listed in table 4. It is found that the fresh PM–PZ(a) catalyst shows the highest catalytic activity for the reduction of NO and the oxidation of CO and C_3H_6. The catalysts containing PCZ mixed oxides exhibit almost the same light-off temperature for the three pollutants, about 10 °C lower than those of PM–CZ. However, the situation is quite different for the catalysts aged at 850 °C for 2 h in atmosphere. An obvious deactivation was found for the catalyst PM–PZ(a). For the catalysts containing PCZ mixed oxides, the light-off temperature becomes higher and higher as praseodymium content increases. However, the aged PM–PCZ(1/21) catalyst possesses the lowest light-off temperature of C_3H_6 and NO. For the three catalysts containing PZ mixed oxide with different preparation procedure, the catalyst PM–PZ(b) shows the highest catalytic performance after being aged at 850 °C.

The conversions of CO, C_3H_6 and NO were also measured for the aged catalysts when the S values varied from 0.96 to 1.07 at constant reaction temperature of 400 °C. Figure 5 reports the NO conversion at different S value for the aged PM–CZ, PM–PZ(a) and PM–PCZ(1/5) catalysts. In this region, conversions of CO and C_3H_6 can reach 100% for all the catalysts. The width of the S value at NO conversion(%) $\geq$ 80% under oxidizing conditions ($S \geq 1.00$) is also listed in table 4. It is observed that all the catalysts containing praseodymium obviously exhibit more effectiveness for NO conversion with the enhanced width of the S value at the lean region ($S \geq 1.00$).

Several factors may result in the deactivation of the aged catalysts containing PZ, such as the sintering, oxidation of the precious metals and the interactions of the components in the catalysts. They can be described as the interactions between praseodymium and γ-alumina support, between praseodymium and PMs, and between PMs and γ-alumina support. The different preparation procedures lead to various intensities of the three kinds of interactions. The interaction between PMs and γ-alumina support occurs for all the catalysts. Because of the drastic phase transition of $(Pr–Zr)O_2$, the catalyst PM–PZ(a) involves strong $Pr–Al_2O_3$ and Pr–PMs interactions during calcination at 850 °C. The $(Pr–Zr)O_2$, Al_2O_3 and γ-Al_2O_3 were calcined at 850 °C prior to the impregnation of precious metals for the PM–PZ(b) catalyst, which may maintain the $Pr–Al_2O_3$ interaction and eliminate the Pr–PMs interaction. For the catalyst PM–PZ(c), only the PZ mixed oxide was calcined at 850 °C prior to the other procedures, which makes both the $Pr–Al_2O_3$ and Pr–PMs interactions eliminated. In table 4, it is observed that the light-off temperatures of PM–PZ(b) are about 40 °C lower than those of PM–PZ(a) and about 20 °C lower than those

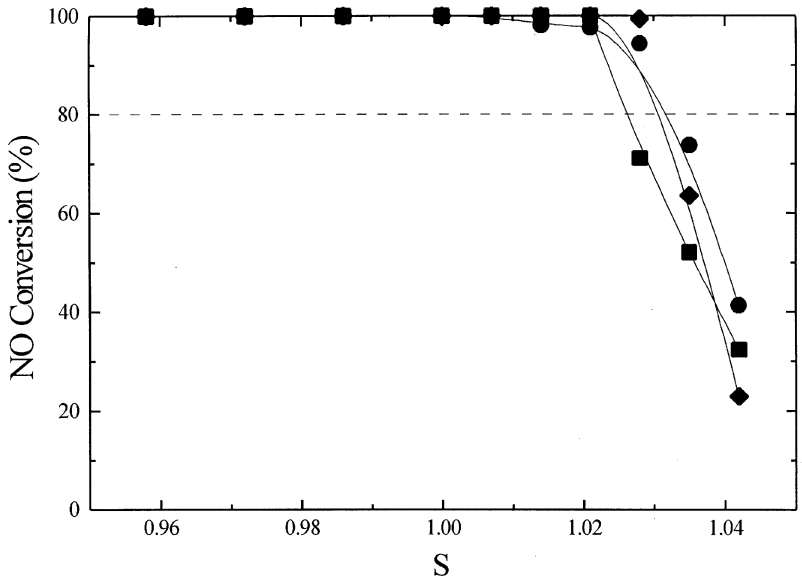

Figure 5. NO conversion at different S values for the aged catalysts: (■) PM–CZ; (◆) PM–PZ(a); (●) PM–PCZ(1/5).

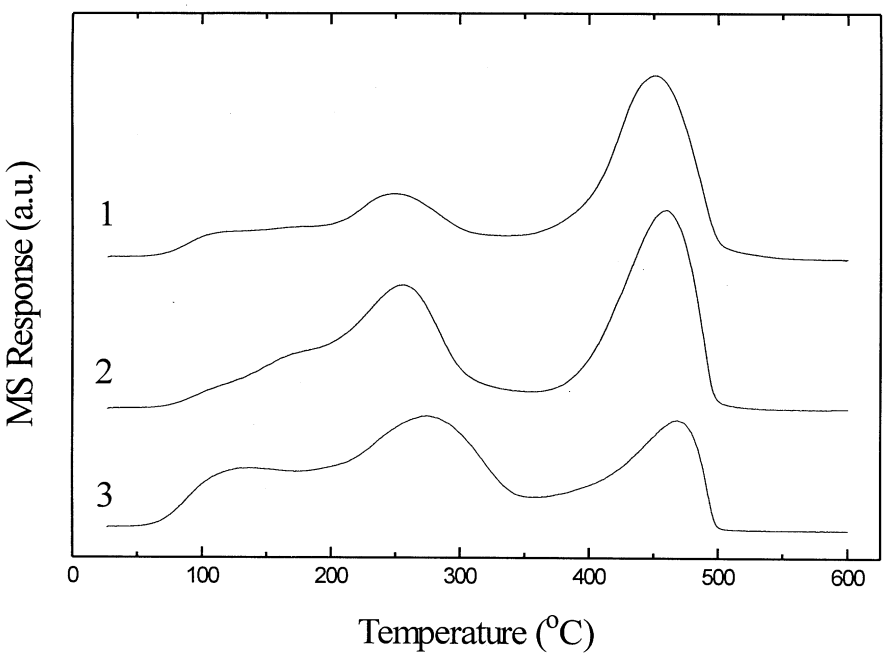

Figure 6. NO–TPD curves for the aged catalysts: (1) PM–CZ; (2) PM–PCZ(1/5); (3) PM–PZ(a). Aging conditions: calcination at 850 °C for 2 h in atmosphere.

of PM–PZ(c). It is believed that the Pr–PMs interaction may strongly deactivate the catalyst and the $Pr–Al_2O_3$ interaction may promote the activities to some extent.

3.5. NO–TPD of the catalysts

TPD curves for NO desorption from the aged catalysts are shown in figure 6. No other nitrogen oxide desorption peak but NO was detected by a mass spectrometer. There is only one desorption peak below 200 °C for the support γ-alumina impregnated with precious metals (not shown). All three curves feature three desorption peaks around <200, 260 and 450 °C. It is suggested that there are three kinds of NO adsorption sites existing on the catalyst surface. The desorption peaks below 200 °C may be attributed to the NO physical adsorption species on the surface, while two kinds of doping adsorption with different intensity are associated with the desorption peaks located around 260 and 450 °C, respectively. The relative intensity of the three peaks varies for the different catalysts. The desorption peak around 450 °C is the strongest one for the PM–CZ and PM–PCZ(1/5) catalysts, while the peak at moderate temperature about 260 °C dominates others for the PM–PZ(a) catalyst.

Table 5
Relative ratio of NO desorption amount at different temperature ranges

Catalyst [a]	NO desorption [b]			
	Total	Below 200 °C	Around 260 °C	Around 450 °C
PM–CZ	1.00	0.14	0.28	0.58
PM–PCZ(1/5)	1.20	0.19	0.45	0.56
PM–PZ(a)	1.14	0.20	0.62	0.32

[a] Catalyst calcined at 850 °C for 2 h in atmosphere.
[b] Desorption integrated by multiple Gaussian fit.

Table 5 lists the relative amount of NO desorption by integrated peak areas of the TPD profiles and the proportion of NO desorption at different temperature range by multiple Gaussian fit. We assume the total desorption amount of catalyst PM–CZ as 1.00 and calculate the other values. The desorption peak at about 260 °C is associated with a medium-intensity NO adsorption on the surface. The catalysts containing praseodymium exhibit enhanced NO desorption at about 260 °C. It is supposed that the medium-intensity NO adsorption favors the catalytic reduction for the NO conversion, which may be beneficial to the broader width of the *S* value.

4. Conclusions

In summary, the present investigation has identified the important role of the Pr dopant in improving the oxygen exchange at low temperatures in the $(Ce–Zr)O_2$ mixed oxide. The $(Pr–Zr)O_2$ mixed oxide can form the cubic solid solution up to 800 °C, while $(Ce–Zr)O_2$ does so at 500 °C by the sol-gel method. The $(Pr–Zr)O_2$ solid solution is more reducible than the $(Ce–Zr)O_2$ solid solution. $(Pr–Ce–Zr)O_2$, $(Ce–Zr)O_2$ and highly dispersed $(Pr–Zr)O_2$ solid solution phases may co-exist in the ternary $Pr_yCe_xZr_{1-x-y}O_2$ mixed oxides calcined at 850 °C.

It is believed that the introduction of a small ratio ($\leq$3% atomic ratio) of praseodymium into $(Ce–Zr)O_2$

favors the light-off temperature of the conversions of C_3H_6 and NO, while a large ratio ($\geq$11% atomic ratio) of praseodymium will affect the thermal stability and the activity of the catalyst. The Pr–PM interaction may result in strong deactivation of the catalysts.

Acknowledgments

This work was supported by the Ford–China Research and Development Fund (No. 9712301) and by BSFR (Beijing Synchrotron Radiation Facility).

References

[1] H.S. Gandhi and M. Shelef, Stud. Surf. Sci. Catal. 30 (1987) 199.
[2] G. Kim, Ind. Eng. Chem. Prod. Res. Dev. 21 (1982) 267.
[3] B. Harrison, A.F. Diwell and C. Hallett, Plat. Met. Rev. 32 (1988).
[4] K.C. Taylor, Catal. Rev. Sci. Eng. 35 (1993) 457.
[5] S.J. Schmieg and D.N. Belton, Appl. Catal. B: Environmental 6 (1995) 127.
[6] J.Z. Shyu, W.H. Weber and H.S. Gandhi, J. Phys. Chem. 92 (1988) 4962.
[7] J.G. Nunan, M.J. Cohn and J.T. Donner, Catal. Today 14 (1992) 277.
[8] S. Bernal, G. Blanco, M.A. Cauqui, G.A. Cifredo, J.M. Pintado and J.M. Rodriguez-Izquierso, Catal. Lett. 53 (1998) 51.
[9] M. Pijolat, M. Prin, M. Soustelle, O. Touret and P. Nortier, J. Chem. Soc. Faraday Trans. 91 (1995) 3941.
[10] A. Trovarelli, F. Zamar, J. Llorca, C. De Leitenburg, G. Dolcetti and J.T. Kiss, J. Catal. 169 (1997) 490.
[11] F. Zamar, A. Trovarelli, C. De Leitenburg and G. Dolcetti, J. Chem. Soc. Chem. Commun. (1995) 965
[12] A. Suda, T. Kandori, N. Terao, Y. Ukyo, H. Sobukawa and M. Sugiura, J. Mater. Sci. Lett. 17 (1998) 89.
[13] M. Hasegawa, Y. Kato, M. Kagawa and Y. Syono, J. Mater. Sci. Lett. 15 (1996) 1608.
[14] P. Vidmar, P. Fornasiero, J. Kaspar, G. Gubitosa and M. Graziani, J. Catal. 171 (1997)160.
[15] A.K. Bhattacharya, A. Hartridge, K.K. Mallick and J.L. Woodhead, J. Mater. Sci. 31 (1996) 5005.
[16] P. Fornasiero, G. Balducci, R. Dimonte, J. Kaspar, V. Sergo, G. Gubitosa, A. Ferrero and M. Graziani, J. Catal. 164 (1996) 173.
[17] A.D. Logan and M. Shelef, J. Mater. Res. 9 (1994) 468.
[18] C.K. Narula, L.P. Hacck, W. Chu, H.-W. Jen and G.W. Graham, J. Phys. Chem. B 103 (1999) 3634
[19] E.S. Putna, J.M. Vohs, R.J. Gorte and G.W. Graham, Catal. Lett. 54 (1998) 17.
[20] L. Xiao, P.Y. Lin, W.D. Wang, Z.B. Yang, Y.L. Fu and S.M. Yu, Topics Catal. 16/17 (2001) 107.
[21] D.E. Sayers and B.A. Bunker, in: *X-Ray Absorption: Principles, Applications, Techniques of EXAFS, SEXAFS and XANES*, eds. D.C. Koningsberger and R. Prins (Wiley, New York, 1988), p. 211.
[22] J.G. Nunan, W.B. Willioamson and H.J. Robota, SAE paper No. 960798.
[23] P. Fornasiero, R. Monte, G.R. Rao, J. Kaspar, A. Trovarelli and M. Graziani, J. Catal. 151 (1995) 168.
[24] B.K. Cho, J. Catal. 131 (1991) 74